

Standing in the shadow of dark gas: ALMA observations of absorption from dark CO in the molecular dark neutral medium of Chamaeleon

H. Liszt, M. Gerin, I. Grenier

▶ **To cite this version:**

H. Liszt, M. Gerin, I. Grenier. Standing in the shadow of dark gas: ALMA observations of absorption from dark CO in the molecular dark neutral medium of Chamaeleon. Astronomy and Astrophysics - A&A, 2019, 627, pp.A95. 10.1051/0004-6361/201935436 . cea-02175850

HAL Id: cea-02175850

https://cea.hal.science/cea-02175850

Submitted on 6 Jul 2019

HAL is a multi-disciplinary open access archive for the deposit and dissemination of scientific research documents, whether they are published or not. The documents may come from teaching and research institutions in France or abroad, or from public or private research centers.

L'archive ouverte pluridisciplinaire **HAL**, est destinée au dépôt et à la diffusion de documents scientifiques de niveau recherche, publiés ou non, émanant des établissements d'enseignement et de recherche français ou étrangers, des laboratoires publics ou privés.

A&A 627, A95 (2019)
https://doi.org/10.1051/0004-6361/201935436
© ESO 2019

Astronomy & Astrophysics

Standing in the shadow of dark gas: ALMA observations of absorption from dark CO in the molecular dark neutral medium of Chamaeleon⋆

H. Liszt[1], M. Gerin[2], and I. Grenier[3]

[1] National Radio Astronomy Observatory, 520 Edgemont Road, Charlottesville, VA 22903, USA
e-mail: hliszt@nrao.edu
[2] LERMA, Observatoire de Paris, PSL Research University, CNRS Sorbonne Universités, UPMC Université Paris 06, Ecole Normale Supérieure, 75005 Paris, France
[3] Département d'Astrophysique, AIM, CEA-IRFU/CNRS/Université Paris Diderot, CEA, Saclay, 91191 Gif-sur-Yvette, France

Received 8 March 2019 / Accepted 1 May 2019

ABSTRACT

Context. We previously detected 89.2 GHz $J = 1-0$ HCO^+ absorption in 12 directions lacking detected CO emission in the outskirts of the Chamaeleon cloud complex and toward one sightline with integrated CO emission $W_{CO} = 2.4$ K km s^{-1}. Eight sightlines had a much larger mean column density of dark neutral medium (DNM) – gas not represented in HI or CO emission – and were found to have much higher mean molecular column density. The five other sightlines had little or no DNM and were found to have much smaller but still detectable $N(HCO^+)$.

Aims. To determine the CO column density along previously observed Chamaeleon sightlines and to determine why CO emission was not detected in directions where molecular gas is present.

Methods. We took ^{12}CO $J = 1-0$ absorption profiles toward five sightlines having higher DNM and HCO^+ column densities and one sightline with smaller N(DNM) and $N(HCO^+)$. We converted the integrated HCO^+ optical depths to $N(H_2)$ in the weak-excitation limit using $N(HCO^+)/N(H_2) = 3 \times 10^{-9}$ and converted the integrated CO optical depths Υ_{CO} to CO column density using the relationship $N(CO) = 1.861 \times 10^{15}$ cm$^{-2}\Upsilon_{CO}^{1.131}$ found along comparable lines of sight that were previously studied in $J = 1-0$ and $J = 2-1$ CO absorption and emission.

Results. CO absorption was detected along the five sightlines in the higher-DNM group, with CO column densities 4×10^{13} cm$^{-2} \lesssim N(CO) \lesssim 10^{15}$ cm^{-2} that are generally below the detectability limit of CO emission surveys.

Conclusions. In the outskirts of the Chamaeleon complex, the presence of molecular DNM resulted primarily from small CO column densities at the onset of CO formation around the HI/H_2 transition in diffuse molecular gas. CO relative abundances $N(CO)/H_2 \lesssim 2 \times 10^{-6}$ in the outskirts of Chamaeleon are comparable to those seen in UV absorption toward early-type stars, including in Chamaeleon.

Key words. ISM: molecules – dust, extinction – ISM: clouds

1. Introduction

The total gas column densities that are jointly traced by dust and by cosmic-ray interactions exhibit large excesses over those inferred from HI and CO line emission in galactic molecular cloud complexes (Grenier et al. 2005), including in Chamaeleon (Planck Collaboration Int. XXVIII 2015). In a recent paper (Liszt et al. 2018; Paper I) we sought evidence of a hidden molecular gas reservoir in Chamaeleon. We presented observations of absorption from $\lambda 3$ mm $J = 1-0$ lines HCO^+, HCN, and C_2H toward thirteen compact extragalactic continuum sources seen against the outskirts of the Chamaeleon cloud complex. We detected HCO^+ absorption in all directions even though CO emission was firmly detected in only one of these.

Taking an abundance ratio $N(HCO^+)/N(H_2) = 3 \times 10^{-9}$ we compared the inferred column densities of H_2 to those of the dark neutral medium (DNM), the gas inferred to be present from maps of sub-mm dust opacity and gamma-ray emissivity (Planck Collaboration Int. XXVIII 2015; Remy et al. 2018) but not apparently represented in $\lambda 21$ cm HI or $\lambda 2.6$ mm CO line emission. We found that gas in the outskirts of Chamaeleon was mostly atomic (HI rather than H_2) but that the DNM was mostly molecular, resulting from failure of the integrated CO $J = 1-0$ emission W_{CO} to represent the true amount of molecular hydrogen when using a standard CO-H_2 conversion factor $N(H_2)/W_{CO} = 2 \times 10^{20}$ cm^{-2} (K km s^{-1})$^{-1}$. Saturation of the HI emission profile might have contributed significantly to N(DNM) in three directions but did not create the need for the DNM.

Here we ask why CO emission did not represent the molecular gas component adequately: perhaps as the result of inadequate rotational excitation of the CO, or perhaps as the result of there being only very small CO column densities at the onset of CO formation around the HI–H_2 transition. In the present work we observed $\lambda 2.6$ mm $J = 1 - 0$ CO absorption toward six of the thirteen sources observed in our earlier paper, five in the group of eight directions showing more DNM and H_2, and (because it was convenient) one direction in the group of five showing little or no DNM and much smaller but still non-zero $N(HCO^+)$. The integrated CO optical depths are converted to CO column density using the tight relationship defined

⋆ The data are only available at the CDS via anonymous ftp to cdsarc.u-strasbg.fr (130.79.128.5) or via http://cdsarc.u-strasbg.fr/viz-bin/qcat?J/A+A/627/A95

Table 1. Sightline and velocity-integrated spectral line properties.

Source	α(J2000) hh.mmssss	δ(J2000) dd.mmssss	l (°)	b (°)	$E(B–V)$ [a] (mag)	N(HI) [b] 10^{20} cm^{-2}	Υ_{HCO^+} [c] (km s^{-1})	S_{115} (Jy)	$\sigma_{l/c}$ [d]	Υ_{CO} [c] (km s^{-1})
J0942-7731	09.424275	−77.311158	293.321	−18.329	0.33	9.1	1.142(0.067) [e]	0.140	0.126	0.855(0.133)
J1058-8003	10.584331	−80.035416	298.010	−18.288	0.15	6.0	0.201(0.009)	1.684	0.010	0.034(0.008)
J1136-6827	11.360210	−68.270609	296.070	−6.590	0.47	21.7	1.241(0.035)	0.344	0.054	0.396(0.047)
J1145-6954	11.455362	−69.540179	297.316	−7.747	0.38	16.8	0.870(0.031)	0.517	0.034	0.125(0.025)
J1224-8313	12.245438	−83.131010	302.095	−20.391	0.26	8.7	0.945(0.044)	0.132	0.122	0.679(0.137)
B1251-7138	12.545983	−71.381840	303.213	−8.769	0.28	17.0	0.139(0.027)	0.323	0.055	<0.131 [f]

Notes. [a]Schlegel et al. (1998). [b]$N(\mathrm{HI}) = \int T_B\, dv \times 1.823 \times 10^{18}$ cm^{-2} from the Gass III HI profile (Kalberla & Haud 2015). [c]Υ_{HCO^+} and Υ_{CO} are the integrated $J = 1 - 0$ optical depth in units of km s^{-1}. [d]Line/continuum rms at zero optical depth in the 2× oversampled spectrum. [e]Quantities in parenthesis are the standard deviation. [f]Upper limit is 3σ.

along comparable lines of sight previously studied in CO J = 1−0 and J = 2−1 absorption and emission by Liszt & Lucas (1998).

The organization of this paper is as follows. In Sect. 2 we discuss the new and existing observational material that is presented here and give the background of the integrated optical depth – column density conversion for the CO J = 1−0 absorption profiles. Section 3 presents the results of this work and, in Sect. 4, drawing on earlier studies of the excitation of CO, we show that the failure of CO emission to represent $N(H_2)$ is due to small CO column densities N(CO) and relative abundances $N(CO)/N(H_2)$ that are familiar from studies of UV absorption at comparable reddening $E(B–V)$. Section 5 slightly extends the DNM analysis of Paper I using direct UV absorption measurements of $N(H_2)$ and N(CO) toward a handful of stars seen toward Chamaeleon and Sect. 6 is a summary.

2. Observations, data reduction and optical depth–column density conversion

2.1. Conventions

In this work, N(H) is the column density of H-nuclei in neutral atomic and molecular form, $N(H) = N(\mathrm{HI}) + 2N(H_2)$. We denote the observed, integrated J = 1−0 optical depths of the J = 1−0 CO and HCO^+ transitions as $\Upsilon_{CO} = \int \tau_{0,1}(\mathrm{CO})\, dv$ and $\Upsilon_{HCO^+} = \int \tau_{0,1}(HCO^+)\, dv$. Velocities presented with the spectra are measured with respect to the kinematic definition of the Local Standard of Rest.

2.2. New ALMA absorption measurements

We observed the J = 1−0 lines of ^{12}CO and ^{12}CN in absorption toward the six continuum sources whose line of sight properties are given in Table 1; the resulting CO line profiles are shown in Figs. 1 and 2. The work was conducted under ALMA Cycle 5 project 2017.1.00227.S whose pipeline data products were delivered in 2018 February. The spectra discussed here were extracted from the pipeline-processed, continuum-subtracted data cubes at the pixel of peak continuum flux in the continuum map made from each spectral window, and divided by the continuum flux in the continuum map at that pixel. No (further) baselining of any of the spectra was performed. Fluxes at 115.3 GHz ranged from 0.13 Jy for J1224 and 0.140 for J0942 to 1.68 Jy for J1058: several of the sources were considerably dimmer than in our Cycle 4 HCO^+ observations. Each spectrum consisted of 1919 semi-independent channels spaced by 30.503 kHz corresponding to 0.079 km s^{-1} at the 115.271 GHz rest frequency of ^{12}CO. The channel spacing is half the spectral resolution. CN was very tentatively detected in one direction, toward J1224, and will not be further discussed here.

2.3. Other observational data at radio and UV wavelengths

In Table 1 we quote the integrated HCO^+ optical depths from Paper I and the optically thin HI column densities derived from Galactic All-Sky Survey (GASS) III λ21 cm HI emission spectra (Kalberla & Haud 2015). Column densities of HCO^+ are taken from Paper I as derived assuming rotational excitation in equilibrium with the cosmic microwave background, $N(HCO^+) = 1.10 \times 10^{12}$ cm^{-2} Υ_{HCO^+} for a permanent dipole moment μ = 3.89 Debye. Figure 1 shows the NANTEN CO J = 1−0 emission spectra used by Planck Collaboration Int. XXVIII (2015) to derive the column density of DNM along with the CO and HCO^+ absorption profiles taken during the course of our work that are shown in more detail in Fig. 2.

Figure 3 shows the N(CO)–Υ_{CO} relation derived from the prior observations of J = 1−0 and J = 2−1 CO emission and absorption by Liszt & Lucas (1998): this is used to convert our new measurements of Υ_{CO} to N(CO) as discussed in Sect. 4.1. Figure 4 compares CO and H_2 column densities at radio and UV wavelengths using the results of Burgh et al. (2007), Sonnentrucker et al. (2007) and Sheffer et al. (2008).

2.4. Reddening and dust optical depth

The 6′ resolution dust-emission maps scaled to optical reddening $E(B–V)$ by Schlegel et al. (1998) are used in Tables 1 and 4. These reddening values can be converted to Planck 353 GHz dust optical depth τ_{353} with errors of order ±6% using the relationship established by Planck Collaboration XI (2014) between τ_{353} and reddening determined photometrically toward quasars, $E(B–V)/\tau_{353} = (1.49 \pm 0.03) \times 10^4$ mag.

2.5. Conversion from integrated optical depth to column density for CO

Here we measure the integral of the optical depth of the CO J = 1−0 transition Υ_{CO} and additional assumptions are required to convert this to total CO column density. Most generally, the integrated optical depth of the ^{12}CO J, J + 1 transitions are related to the column densities in rotational levels J and J + 1 and the

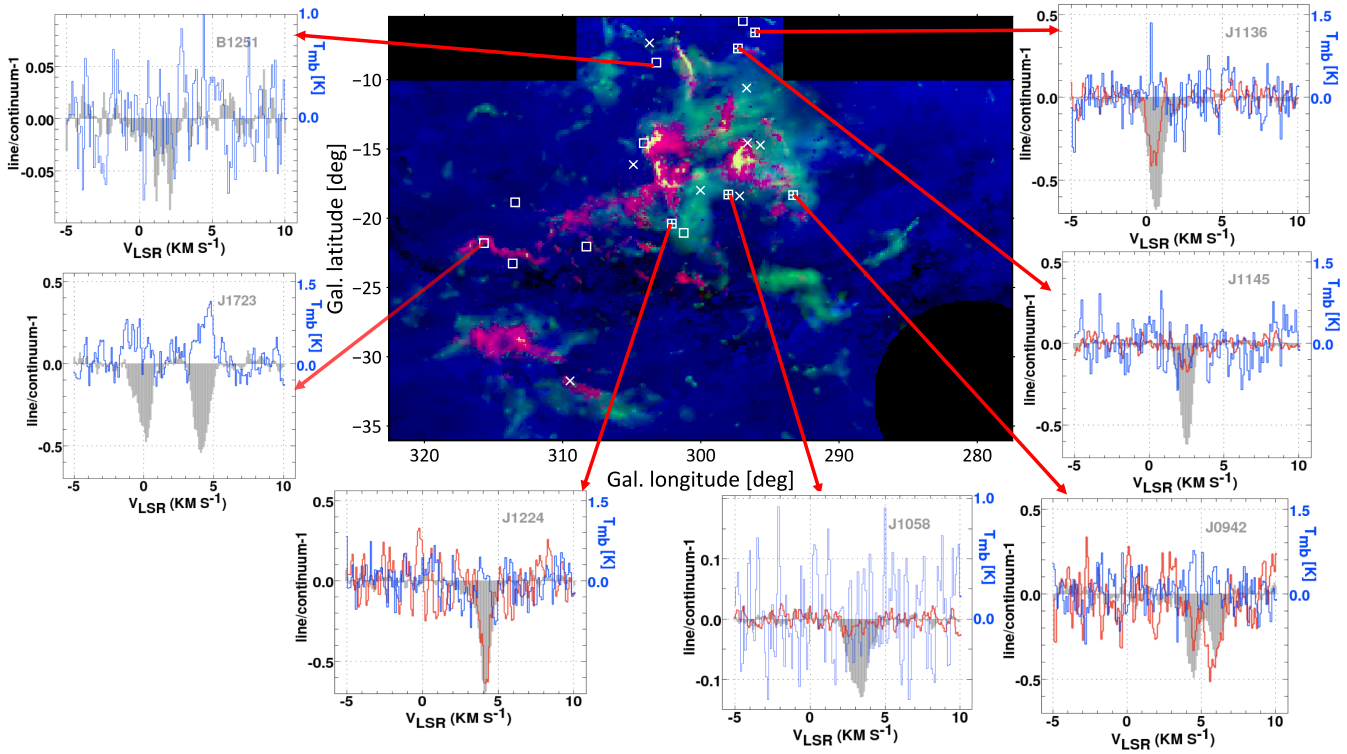


Fig. 1. ALMA results in the Chamaeleon complex. Center: RGB image with N(HI) in blue, N(DNM) in green and Nanten CO emission brightness in red. The locations of the 13 ALMA sources studied in Paper I are marked as squares, hatched for the 5 directions where CO absorption was detected in this work. The positions of 8 stars with measured values of N(H_2) and N(CO) in UV absorption (Table 3) are marked by x's. Shown around the outside are HCO^+ (grey, shaded) and CO (red) absorption and CO emission profiles (blue) from NANTEN on a different vertical scale as noted at right in each outer panel. CO absorption was not observed toward J1723 and was sought but not detected or plotted toward B1251.

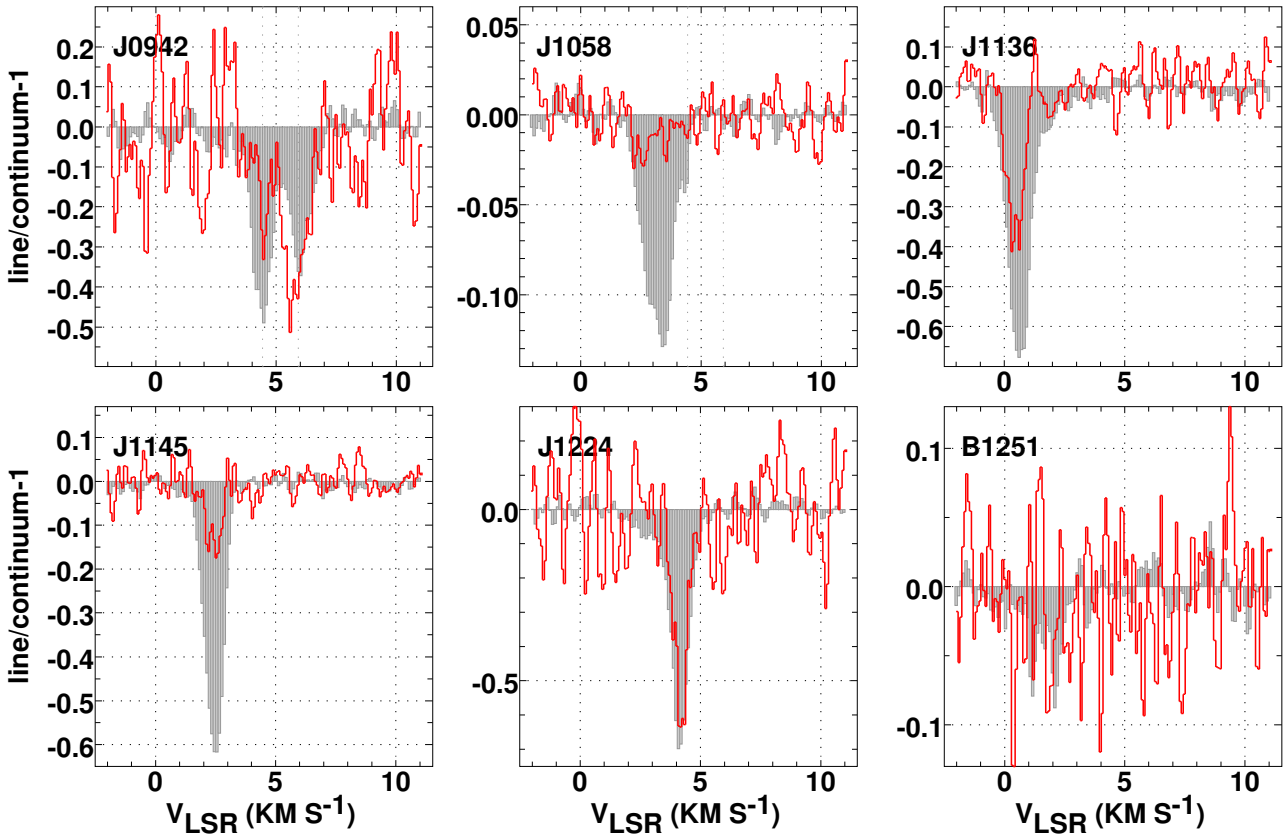


Fig. 2. ALMA HCO^+ and ^{12}CO absorption profiles for the six sources observed here. The HCO^+ profile from Paper I is shown shaded in grey, the ^{12}CO $J = 1-0$ profile from this work is shown in red.

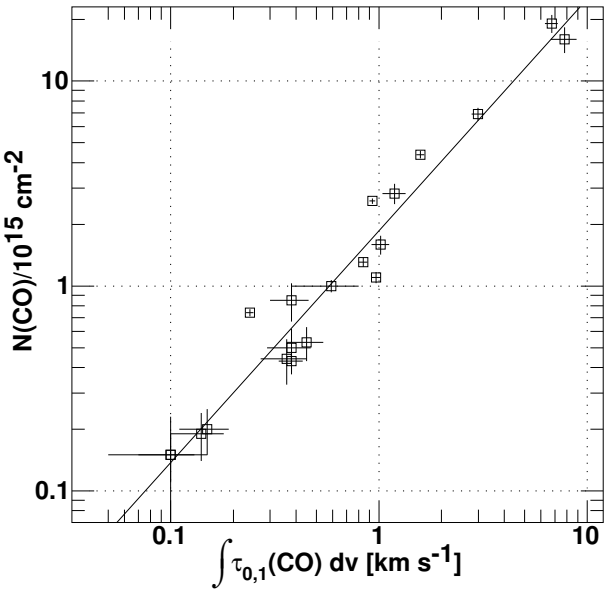


Fig. 3. The relationship between integrated CO $J = 1-0$ optical depth and N(CO) for the data of Liszt & Lucas (1998) who observed $J = 1-0$ and $J = 2-1$ CO emission and absorption along comparable sightlines. The power-law fit is $N(\mathrm{CO}) = 1.861 \times 10^{15}$ cm$^{-2}\Upsilon_{\mathrm{CO}}{}^{1.131}$ where $\Upsilon_{\mathrm{CO}} = \int \tau_{0,1}(\mathrm{CO})\,\mathrm{d}v$ in units of km s^{-1}.

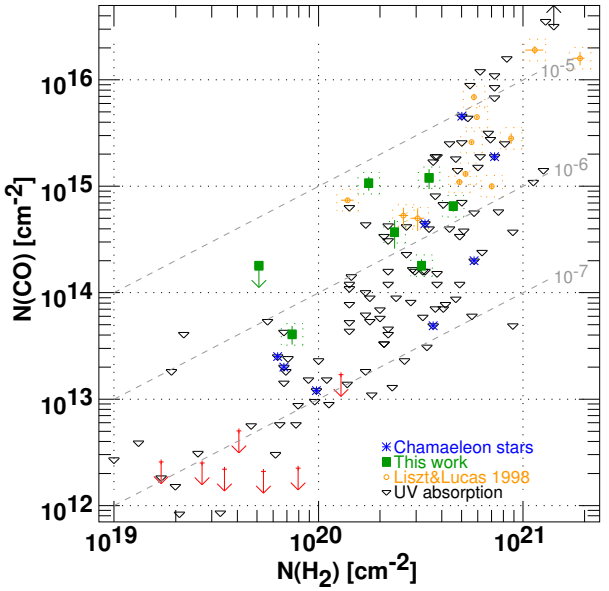


Fig. 4. H_2 and CO column densities from UV and radio absorption spectra. Shown are UV absorption line measurements from Sonnentrucker et al. (2007), Burgh et al. (2007) and Sheffer et al. (2008) (downward-pointing triangles), mm-wave results from Liszt & Lucas (1998) (small orange circles), and results from this work (green filled squares). Some informative upper limits to UV measurements are shown in red. The mm-wave results assume $N(\mathrm{H_2}) = N(\mathrm{HCO^+})/3 \times 10^{-9}$ and the present results use Eq. (2) to derive N(CO). UV absorption sightlines in Chamaeleon are marked by blue asterisks, see Table 4. Grey dashed lines show the locii of relative abundances $N(\mathrm{CO})/N(\mathrm{H_2})$ as indicated. Only sighlines with $N(\mathrm{CO}) > 10^{15}$ cm^{-2} are observable in present wide-field CO emission surveys.

Einstein B-coefficients as

$$\int \tau_{J,J+1}\mathrm{d}v = (h\nu/c)[N_J B_{J,J+1} - N_{J+1}B_{J+1,J}]. \quad (1a)$$

For a linear rotor like CO with a permanent dipole moment $\mu = 0.11$ Debye (1 Debye $= 10^{-18}$ esu) this can be recast as

$$N_J = \frac{(2J+1)}{(J+1)} \frac{6.61 \times 10^{14}\ \mathrm{cm^{-2}} \tau_{J,J+1}}{(\mu/0.11D)^2(1-\exp(-h\nu/kT_{\mathrm{ex}}))}, \quad (1b)$$

where $\int \tau_{J,J+1}\ \mathrm{d}v$ is in units of km s^{-1} and T_{ex} is the excitation temperature between levels J and $J+1$, $N_{J+1}/N_J = (g_{J+1}/g_J)\exp(-h\nu/kT_{\mathrm{ex}})$ and $g_J = 2J+1$.

CO excitation temperatures are directly observed in diffuse molecular gas toward early-type stars (Burgh et al. 2007; Sonnentrucker et al. 2007; Sheffer et al. 2008) and for the $J = 1-0$ transition these are typically in the range 3–5 K (see Fig. 5 of Liszt 2007 and Table 2 of Goldsmith 2013). Similar values are inferred for gas observed in mm-wave CO absorption (Liszt & Lucas 1998). In the simple case of LTE at a single excitation temperature T_{ex} for all J, the total column density can be written $N(\mathrm{CO}) = b\,\Upsilon_{\mathrm{CO}}$, leading to $b = 1.071 \times 10^{15}$ cm^{-2} (km s^{-1})$^{-1}$ for $T_{\mathrm{ex}} = 2.73$K (the lower limit). Other cases include $b = 1.381 \times 10^{15}$ cm^{-2} (km s^{-1})$^{-1}$ for $T_{\mathrm{ex}} = 3.5$ K, $b = 1.614 \times 10^{15}$ cm^{-2} (km s^{-1})$^{-1}$ for $T_{\mathrm{ex}} = 4$ K and $b = 1.871 \times 10^{15}$ cm^{-2} (km s^{-1})$^{-1}$ for $T_{\mathrm{ex}} = 4.5$ K.

Here we convert the observed values of CO $J = 1-0$ optical depths to column density using the earlier results of Liszt & Lucas (1998) who determined N(CO) along similar sightlines using $J = 1-0$ and $J = 2-1$ observations of CO in absorption and emission. Their results for the integrated $J = 1-0$ optical depths and CO column densities are very well represented with a slightly super-linear power-law regression fit as discussed in Sect. 4.1. Given the numerical examples in the preceding paragraph, this is roughly equivalent to assuming an excitation temperature of 4.4–4.5 K for the stronger lines observed here (Table 1). An excitation temperature of at least 4.0 K is required to produce a 1 K brightness in CO $J = 1-0$ emission although a smaller excitation temperature can produce an integrated brightness $W_{\mathrm{CO}} > 1$ K km s^{-1} with a sufficiently wide line.

As discussed by Liszt & Lucas (1998) and Liszt & Pety (2012), the excitation temperature of the CO $J = 1-0$ transition scales directly as the ambient thermal pressure of H_2 and increases with $\tau_{0,1}$. With a $J = 1-0$ excitation temperature of 4.5 K the implied partial pressures of H_2 are $n(\mathrm{H_2})T_{\mathrm{K}} = 5.8 \times 10^3$ and 4.0×10^3 cm^{-3} K for $\tau_{0,1}(\mathrm{CO}) = 0$ and 1, respectively. These are typical values for the diffuse ISM sampled in C I by Jenkins & Tripp (2011).

2.6. The relative abundance of HCO^+

As in Paper I we use the relative abundance $N(\mathrm{HCO^+})/N(\mathrm{H_2}) = 3 \times 10^{-9}$ to derive $N(\mathrm{H_2})$, the $\mathrm{HCO^+}/\mathrm{H_2}$ ratio being assumed to be constant in the gas. This value originates in the tight relationships that exist between HCO^+ and OH (Liszt & Lucas 1996, 2000) or CH (Gerin et al. 2019), both of which are directly measured in optical/UV absorption spectra to have fixed abundances relative to H_2 (Liszt 2007; Sonnentrucker et al. 2007; Sheffer et al. 2008; Weselak et al. 2009, 2010). The overall uncertainty in the abundance of HCO^+ relative to H_2 was estimated by Gerin et al. (2019) to be ±0.2 dex; see their Table 4 giving relative abundances and uncertainties for a variety of molecules used as proxies for H_2 at radio/sub-mm wavelengths.

3. Observational results

General properties of the sightlines observed here are given in Table 1, including HCO^+ and CO optical depths integrated

Table 2. HCO^+ H_2 and CO column densities.

Source	v_0 km s^{-1}	$N(HCO^+)$ [a] 10^{12} cm^{-2}	$N(H_2)$ [b] 10^{20} cm^{-2}	$N(CO)$ [c] 10^{15} cm^{-2}	$N(CO)/N(H_2)$ 10^{-6}
J0942	4.5	0.64(0.02) [d]	2.35	0.37(0.11)	1.56
	6.0	0.48(0.02)	1.76	1.07(0.16)	6.08
J1058	3.2	0.22(0.04)	0.74	0.04(0.01)	0.55
J1136	0.6	1.48(0.04)	4.55	0.65(0.07)	1.42
J1145	2.5	0.96(0.03)	3.19	0.18(0.03)	0.56
J1224	4.0	1.04(0.05)	3.47	1.20(0.26)	3.45
B1251	1.7	0.15(0.03)	0.51	<0.18 [e]	<3.66 [e]
Mean [f]	3.4(1.8)	0.80(0.45)	2.68(1.35)	0.59(0.47)	2.27(2.15)
Mean [g]	3.2(1.8)	0.71(0.48)	2.37(1.48)	0.53(0.46)	2.47(2.02)

Notes. [a]$N(HCO^+) = 1.10 \times 10^{12}$ cm$^{-2} I_{HCO^+}$. [b]$N(H_2) = N(HCO^+)/3 \times 10^{-9}$. [c]$N(CO) = 1.861 \times 10^{15}$ cm$^{-2} I_{CO}^{1.131}$. [d]Quantities in parentheses are the standard deviation. [e]Upper limits are 3σ. [f]For the six components with CO detections. [g]Including B1251 at the upper limit.

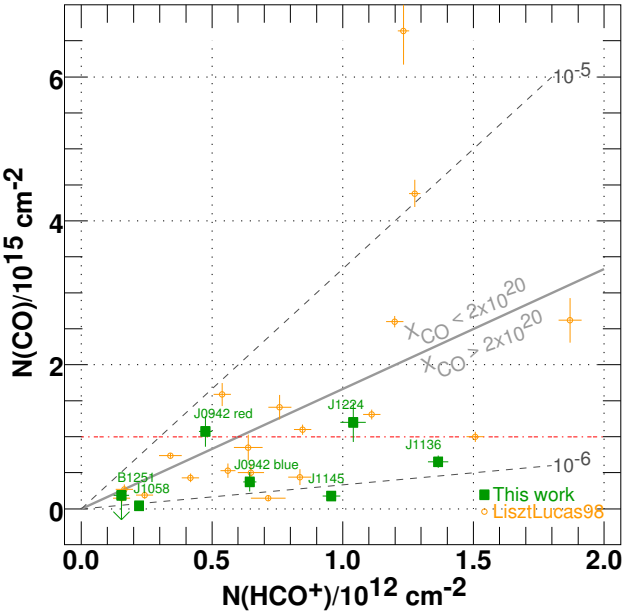


Fig. 5. CO and HCO^+ column densities. Shown are results from this work (larger green filled squares) and the earlier observations of Liszt & Lucas (1998) (small orange circles). Integrated CO $J = 1–0$ optical depths Υ_{CO} have been converted to CO column density using the relationship between Υ_{CO} and $N(CO)$ shown in Fig. 3, $N(CO) = 1.861 \times 10^{15}$ cm^{-2} $\Upsilon_{CO}^{1.131}$. Grey dashed shaded lines show fiducial values $N(CO)/N(H_2) = 10^{-6}$ and 10^{-5} assuming $N(HCO^+)/N(H_2) = 3 \times 10^{-9}$. The broad grey line at $N(CO)/N(H_2) = 5 \times 10^{-6}$ divides the plot area into regions where X_{CO} is larger or smaller than 2×10^{20} H_2 (K km s^{-1})$^{-1}$. The red dash-dotted line at $N(CO) = 10^{15}$ cm^{-2} shows the CO column density at which the integrated $J = 1–0$ emission brightness $W_{CO} = 1$ K km s^{-1}.

over the velocity range of the HCO^+ absorption. Table 2 relates derived values of $N(CO)$, $N(HCO^+)$ and $N(H_2)$ as shown in Figs. 4 and 5. Table 3 shows Gaussian decompositions of the CO profiles in those cases where it is justified, compared with the profile integral and results of Gaussian decomposition of the HCO^+ profiles.

Figure 1 is a finding chart for the thirteen sources observed in HCO^+ absorption, showing their placement on the sky with respect to the distributions of N(HI), N(DNM) and and the integrated CO brightness W_{CO} as derived by Planck Collaboration Int. XXVIII (2015). Sightlines toward 6 of these were observed in CO, and CO and HCO^+ profiles in these directions are shown in panels arranged around the periphery of the chart along with profiles toward J1723 that has detectable CO emission but was not observed in CO absorption in this work.

HCO^+ and CO absorption profiles are shown in Fig. 2 for all the sources observed here. CO absorption was detected along all five of sightlines in the high-DNM group and not toward B1251. The sightline to J0942 has the strongest integrated CO absorption in total but the strongest single feature is at 4 km s^{-1} toward J1224. The detection of very weak CO absorption toward J1058 was only possible because of its very strong continuum flux.

The relative abundances of $N(CO)$ and $N(H_2)$ are known to have very wide variations resulting from their sensitivity to resonant photodissocation (Fig. 4) so it is not surprising that the ratio of the integrated CO and HCO^+ optical depths ranges from 0.7 to 7 among the sightlines measured here (Tables 1 and 3). A mild surprise is that CO absorption is so weak in the blue-shifted component having much stronger HCO^+ absorption toward J0942. The NANTEN spectrum toward J0942 (Fig. 1) suggested the possible presence of CO emission overlapping the HCO^+ absorption and with stronger emission to the blue, in the same sense as that of the HCO^+ absorption. This work shows that the CO column density in the blue-shifted component toward J0942 is too small to support a CO detection in emission.

4. CO and H_2 column densities, CO brightness and CO-H_2 conversion factor

4.1. Υ_{CO}, $N(CO)$ and W_{CO}

Figure 3 shows the data of Liszt & Lucas (1998) leading to the regression relation that we use to convert the CO $J = 1–0$ integrated optical depth Υ_{CO} to column density $N(CO)$ as discussed in Sect. 2.5.

$$N(CO) = 1.861 \times 10^{15} \text{ cm}^{-2} \Upsilon_{CO}^{1.131}. \quad (2)$$

Table 2 gives the results of using Eq. (2) and $N(H_2) = N(HCO^+)/3 \times 10^{-9}$ to derive $N(CO)$ and $N(H_2)$ from our mm-wave CO and HCO^+ absorption measurements. As a check on this procedure, Fig. 4 compares the present and prior mm-wave results for $N(CO)$ and $N(H_2)$ with the larger sample of direct UV absorption line measurements of Sonnentrucker et al. (2007), Burgh et al. (2007) and Sheffer et al. (2008). Results for UV sightlines in the Chamaeleon region are noted in Fig. 4 (see Table 4) and are not exceptional.

The mm-wave results appear typical, not outliers, lending confidence to the assumed relative abundance of HCO^+ that was used to derive $N(H_2)$. The mean relative abundance $\langle N(CO)/N(H_2) \rangle \simeq 2.2–2.5 \times 10^{-6}$ for the lines of sight observed here (Table 2) is very small compared to the expected fractional abundance of free gas-phase carbon, $N(C)/N(H) \simeq 1.6 \times 10^{-4}$ (Sofia et al. 2004), but still larger than found along many of the sightlines represented by UV absorption in Fig. 4. The older mm-wave results of Liszt & Lucas (1998) have CO and H_2 column densities toward the upper ends of their respective distributions in Fig. 4, and stronger ^{13}CO fractionation than is typically the case for the UV measurements (Liszt 2017).

In Fig. 5 we compare $N(CO)$ and $N(HCO^+)$ from the present work with those in the earlier study of CO in emission

Table 3. Gaussian decomposition of HCO^+ and CO absorption.

	HCO^+	HCO^+	HCO^+	HCO^+	CO	CO	CO	CO
Source	v_0 km s^{-1}	τ_0	$FWHM$ km s^{-1}	Υ_{HCO^+} km s^{-1}	v_0 km s^{-1}	τ_0	$FWHM$ km s^{-1}	Υ_{CO} km s^{-1}
J0942	4.478	0.634	0.846	0.571	4.494	0.347	0.368	0.136
±	0.029	0.046	0.069	0.040	0.056	0.118	0.128	0.043
	6.045	0.402	1.009	0.432	5.766	0.568	1.046	0.632
±	0.040	0.035	0.098	0.036	0.064	0.086	0.149	0.085
J1058	3.236	0.134	1.409	0.201				
±	0.014	0.003	0.035	0.004				
J1136	0.607	1.100	0.938	1.098	0.449	0.507	0.704	0.380
±	0.007	0.022	0.017	0.019	0.022	0.038	0.048	0.025
	1.880	0.104	0.684	0.076				
±	0.042	0.011	0.101	0.009				
J1145	2.501	0.938	0.809	0.808	2.426	0.171	0.701	0.128
±	0.009	0.030	0.019	0.021	0.042	0.022	0.097	0.016
J1224	3.741	0.127	2.261	0.307				
±	0.149	0.025	0.287	0.047				
	4.218	0.979	0.643	0.670	4.215	0.975	0.481	0.500
±	0.012	0.068	0.028	0.036	0.057	0.169	0.113	0.094

Table 4. Stars toward Chamaeleon studied in UV absorption.

Star HD/CPD	l (°)	b (°)	Distance (pc)	$E(B–V)_*$ (mag)	$E(B–V)_{SFD}^{(a)}$ (mag)	$N(H_2)$ 10^{20} cm^{-2}	$N(CO)$ 10^{14} cm^{-2}
−69 1743	303.71	−7.35	4700	0.30	0.29	1.00	0.12
93237	297.18	−18.39	310	0.09	0.11	0.63	0.25
94454	295.60	−14.73	330	0.18	0.31	5.75	2.00
96675	296.62	−14.57	160	0.30	0.64	7.24	19.1
99872	296.69	−10.62	230	0.36	0.38	3.31	4.47
102065 [b]	300.03	−18.00	170	0.17	0.38	3.63	0.49
116852 [b]	304.08	−16.13	4800	0.21	0.22	0.68	0.20
203532	309.46	−31.74	250	0.28	0.34	5.00	45.71

Notes. Stellar quantities from Sheffer et al. (2008). [a]Reddening from Schlegel et al. (1998). [b]Also observed by Burgh et al. (2007).

and absorption (Liszt & Lucas 1998). The smaller sample of new data lacks individual features with column densities $N(CO) > 2 \times 10^{15}$ cm^{-2} or $N(HCO^+) > 1.5 \times 10^{12}$ cm^{-2} as found in the older data but results for the two datasets largely overlap.

4.2. The implied CO-H_2 conversion factor

Also plotted in Fig. 5 are dashed lines corresponding to relative abundances $N(CO)/N(H_2) = 10^{-6}$ and 10^{-5}, which follow directly from the relative abundance $N(HCO^+)/N(H_2) = 3 \times 10^{-9}$. An implied CO-$H_2$ conversion factor can be derived when it is recognized that the integrated $J = 1–0$ emission profile brightness W_{CO} is related to $N(CO)$ as $W_{CO}/(1\,K\,km\,s^{-1}) = N(CO)/10^{15}$ cm^{-2} over a wide range of hydrogen number density in diffuse molecular gas (Liszt 2007, 2017), maintaining a high degree of linearity up to brightnesses $W_{CO} \lesssim 5$–$10\,K\,km\,s^{-1}$. In this case the CO-H_2 conversion factor depends only on the relative abundance $N(CO)/N(H_2)$ and the relative abundance $N(CO)/N(H_2) = 5 \times 10^{-6}$ divides Fig. 5 (and the rest of the very local Universe) into regions where the CO-H_2 conversion factor is larger or smaller than 2×10^{20} cm^{-2} (K km s^{-1})$^{-1}$. That this value of the CO-H_2 conversion factor is reached at such low CO/H_2 relative abundances is a consequence of the very high brightnesses per molecule that occur when the rotational excitation is so strongly sub-thermal (Goldreich & Kwan 1974; Liszt et al. 2010).

Only in the red-shifted component toward J0942 is the implied CO-H_2 conversion factor $N(H_2)/W_{CO}$ below 2×10^{20} H_2 cm^{-2} (K km s^{-1})$^{-1}$. We did not observe CO absorption toward J1723, but consideration of the detected CO emission and HCO^+ absorption in this direction (Fig. 2) provides an interesting point of comparison. Directly integrating over the separate velocity ranges of the two kinematic components results in CO integrated brightnesses of $W_{CO} = 0.90 \pm 0.14$ and 1.36 ± 0.14 K km s^{-1} and HCO^+ integrated optical depths $\Upsilon_{HCO^+} = 0.70 \pm 0.03$ and 0.81 ± 0.03 km s^{-1}. Converting Υ_{HCO^+} to $N(HCO^+)$ and $N(H_2) = N(HCO^+)/3 \times 10^{-9}$ leads to CO-H_2 conversion factors $N(H_2)/W_{CO} = 2.8 \pm 0.5$ and $2.2 \pm 0.2 \times 10^{20}$ H_2 cm^{-2} (K km s^{-1})$^{-1}$ or $N(H_2)/W_{CO} = 2.4 \pm 0.3 \times 10^{20}$ H_2 cm^{-2} (K km s^{-1})$^{-1}$ overall.

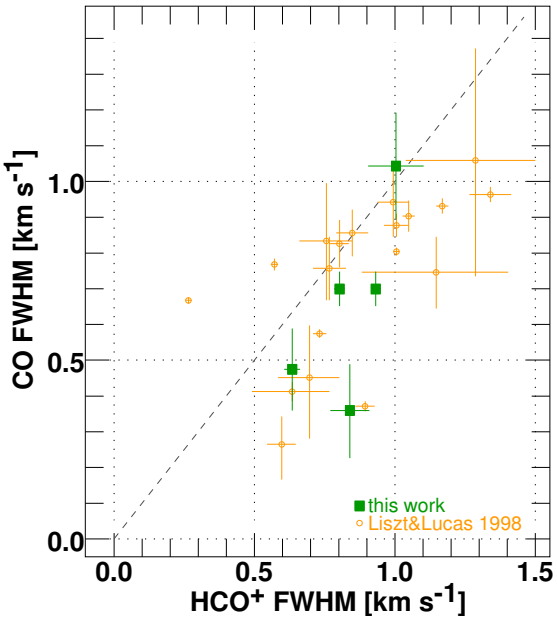


Fig. 6. CO and HCO^+ line profile FWHM. Shown are results from this work (larger green filled squares) and the earlier observations of Liszt & Lucas (1998) (small orange circles). The dashed gray line represents equality of the FWHM.

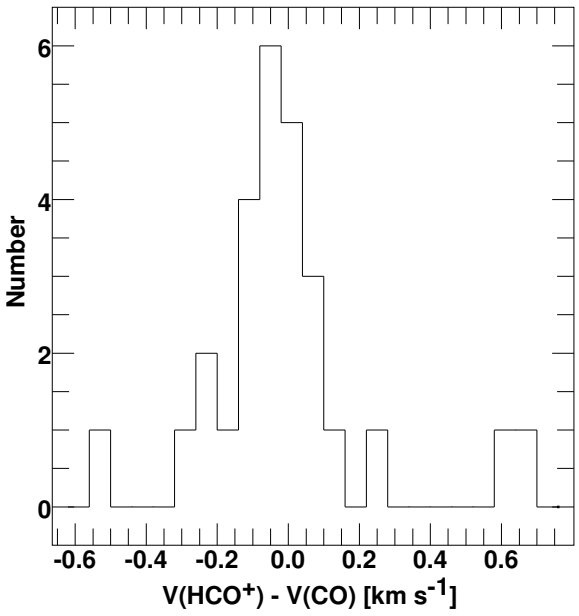


Fig. 7. Distribution of velocity differences between HCO^+ and CO kinematic components from this work and the earlier observations of Liszt & Lucas (1998). The mean difference and its dispersion are 0.10 km s^{-1} ± 0.40 km s^{-1}.

4.3. Kinematics of CO absorption features

In Figs. 4 and 5 we showed that the column densities of CO and HCO^+ in the outskirts of Chamaeleon are like those previously observed along random lines of sight through the diffuse ISM generally and the same is true of the linewidths. In Table 3 we show the results of Gaussian decomposition of the HCO^+ and CO line profiles that are shown in Fig. 2. In some cases the superior signal/noise of the HCO^+ measurements allows fitting of wings and closely-separated components that is not feasible in CO. The plotted results represent only those features that can be identified and associated in both species and have been corrected by quadrature differencing of the FWHM and velocity resolution. The FWHM linewidths for CO are systematically smaller than those of HCO^+ as shown in Fig. 6. The unweighted mean linewidths for the combined sample of new and old data are 0.87 ± 0.24 km s^{-1} for HCO^+ and 0.72 ± 0.22 km s^{-1} for CO. This is not necessarily expected since CO forms from the recombination of HCO^+ in diffuse molecular gas (Glassgold & Langer 1976; Liszt 2007; Visser et al. 2009) and is initially cospatial with parent HCO^+ molecules. HCO^+ and OH profiles do not show comparable differences (Liszt & Lucas 2000). However, recombination of HCO^+ to CO is sensitive to temperature while survival of the CO molecules after formation depends on shielding by H_2, dust and other CO molecules (Draine & Bertoldi 1996; Visser et al. 2009; Sternberg et al. 2014; Liszt 2015), raising the possibility that regions with differing $N(HCO^+)/N(CO)$ exist within the gas and are superposed along the line of sight (Godard et al. 2009).

Linewidth differences among other chemical species are well-known in diffuse molecular gas. In optical spectra there is a sequence CH^+, CH, CN from broader to narrower lines (Lambert et al. 1990; Crane et al. 1995; Pan et al. 2005) perhaps extending further to CO (Pan et al. 2005). At mm-wavelengths, CN absorption lines are narrower than those of HCN and HNC (Liszt & Lucas 2001; Godard et al. 2010) from which CN forms by photodissociation, and all the CN-bearing species have narrower lines than in HCO^+. CH^+ lines are typically much wider than those of other molecules, presumably because the formation of CH^+ occurs through the strongly endothermic reaction of C^+ and H_2. HCO^+ may keep a memory of this excess kinetic energy seen in the CH^+ linewidth because it is such a close daughter product of CH^+ (Godard et al. 2014).

Linewidth differences could arise as the result of the interplay between chemistry and gas dynamics in the diffuse molecular gas but not because CO molecules in the line wings of mm-wave absorption profiles are more susceptible to photodissociation. The shielding and self-shielding of H_2 and CO arise from the continuous opacity of dust and the wings of strongly-damped H_2 and CO electronic transitions at the column densities needed to form the observed amounts of CO, and the Doppler velocity distribution of CO or H_2 molecules is not important to their survival.

In Paper I we noted a kinematic segregration in the Chamaeleon gas in the sense that the directions with less DNM and small $N(H_2)$ were seen in HCO^+ only at $v \lesssim 2$ km s^{-1} while the material with velocities 2–6 km s^{-1} had the preponderance of the HCN absorption, stronger HI emission and much more DNM and H_2. We suggested that this might indicate the presence of slow shocks in the region. The CO data in Chamaeleon are too limited to draw firm conclusions but Fig. 7 shows a histogram of the distribution of line centroid velocity differences between HCO^+ and CO for the new and old data. The mean difference is 0.1 km s^{-1}, with a dispersion of 0.4 km s^{-1}, indicating at most a very small systematic shift, and a small but physically significant dispersion.

Dynamical processes are important for the formation chemistry of the molecules we observe, most obviously for HCO^+ whose observed abundance in diffuse molecular gas $N(HCO^+)/N(H_2) = 3 \times 10^{-9}$ is nearly 100 times higher than would be expected from Langevin rates for the reaction of C^+ + OH with their observed column densities (Van Dishoeck & Black 1986). Flower & Pineau des Forets (1998) and Lesaffre et al. (2013) discussd how a collection of slow shocks in magnetized diffuse

gas could produce CH^+, HCO^+ and CO. Most models that boost the CH^+ and/or HCO^+ chemistry in diffuse gas tap the energy of an ion-neutral drift (Valdivia et al. 2017) which has a broad distribution ranging from 0.01 to 1 km s^{-1}. Visser et al. (2009) drew on an earlier model of Federman et al. (1996), calculating molecular abundances at a suprathermal effective temperature determined by an Alven velocity of 3.5 km s^{-1}.

The turbulent dissipation region (TDR) model of diffuse cloud chemistry (Godard et al. 2014) draws on earlier work (Falgarone et al. 1995; Joulain et al. 1998; Pety & Falgarone 2000) and forms CH^+ and HCO^+ in highly localized regions (vortices) where turbulent energy is dissipated and the ion-neutral drift is maximum. HCO^+ subsequently relaxes and accumulates at the observed abundance in ambient gas where it thermalizes and recombines to CO. CO is subsequently fractionated by C^+ exchange at ambient kinetic temperature (Liszt 2017) and both HCO^+ and CO are observed with a degree of rotational excitation that is characteristic of the typical thermal pressures for the diffuse interstellar medium at large (Jenkins & Tripp 2011), as noted in Sect. 2.5. In such a model HCO^+ recombines to CO more rapidly as it thermalizes, and the HCO^+–CO linewidth difference is presumably a collateral effect.

Comparable linewidth differences are expected between HCO^+ and other species that form by the recombination of ions, for instance HCN, HNC and CN that form from recombination of the as-yet undetected species $HCNH^+$. Godard et al. (2010) observed smaller linewidths in HCN and HNC compared to HCO^+ (Liszt & Lucas 2001 did not), and there is general agreement that the smallest linewidths have generally been observed in CN. We sought but did not detect CN except marginally toward J1224. The difference in the velocity profiles therefore appear to be related to the interplay of chemical and dynamical processes controlling the formation of molecules. To explore further the origin of the difference in velocity profiles more data are needed in specific regions where the large-scale orientation of the gas flows and magnetic field are homogeneous.

5. Molecular, missing, and CO-dark gas

In Paper I we showed that HCO^+ absorption lines traced important H_2 reservoirs extending several parsecs beyond the CO-bright parts of the Chamaeleon molecular clouds. The H_2 column densities inferred from the HCO^+ data for a standard abundance ratio $N(HCO^+)/N(H_2) = 3 \times 10^{-9}$ could substantially account for the excess gas along the eight sight lines with large DNM column densities $N(\mathrm{DNM}) \gtrsim 2 \times 10^{20}$ cm^{-2}: diffuse H_2 partially contributed to the DNM toward three directions and fully explained the DNM toward the five densest directions. In this section we extend some of the analysis from Paper I using an expanded, hybrid sample based on direct UV absorption measurements of $N(H_2)$ and $N(CO)$.

In Figs. 1 and 4 we noted the existence of UV absorption measurements of $N(H_2)$ and $N(CO)$ toward stars of widely-varying distance seen toward Chamaeleon (Table 4). The nearer of these stars could in principle lie in front of some portion of the Chamaeleon gas but $N(H_2)$ is actually relatively high for the nearer objects. To complement the modest sample of sightlines observed with ALMA, we extracted the HI and DNM column densities and mm-wave CO brightness W(CO) toward these stars and combined this information with that for the mm-wave sightlines to produce Fig. 8 (like Fig. 6 in Paper I). In Fig. 8 we compare the total hydrogen column density obtained from the dust and gamma-ray data (the x-axis) to the total hydrogen column density $N(HI) + 2N(H_2)$ derived with and without the use of CO emission. In the left panel $N(H_2) = X^0_{CO} W_{CO}$, while at right $N(H_2)$ is measured indirectly from HCO^+ absorption lines for our ALMA data (circles) or directly from UV H_2 absorption lines (crosses). The error bars on $N(H_2)$ at right assume ±25% errors in $N(H_2)$ from the UV data and ±58% errors on the $N(HCO^+)/N(H_2)$ ratio (Liszt & Gerin 2016).

The colour coding with DNM column density shows that diffuse H_2 can fully account for the DNM column densities over a range varying by at least a factor of six. One can also note from the difference in column density scales between the total and DNM gas that the broad atomic envelopes of the clouds contribute more gas along those sight lines than the diffuse H_2 reservoirs. As in Paper I we infer that the DNM is mostly molecular while the gas overall is atomic, for the lines of sight we studied outside the CO-bright portions of the Chamaeleon complex.

6. Summary

Mm-wave CO absorption line measurements are well-suited to detecting or constraining the properties of dark medium and dark CO. The CO absorption measurements performed here answer the question of why the CO emission fails to represent $N(H_2)$ reliably in the outskirts of Chamaeleon. CO column densities and CO relative abundances are small in diffuse molecular gas around the HI → H_2 transition as the result of the CO chemistry at moderate reddening.

In Paper I we detected mm-wave $J = 1-0$ absorption from HCO^+ and, less commonly, C_2H and HCN, against thirteen compact extragalactic continuum sources seen toward the outskirts of the Chamaeleon HII region-molecular cloud complex. Only one of these directions (J1723) had a firm detection of CO $J = 1-0$ emission. Eight of the thirteen directions comprised a group with higher column densities of dark neutral medium and, as we showed, much higher molecular column densities. Converting the $N(HCO^+)$ to $N(H_2)$ with $N(HCO^+)/N(H_2) = 3 \times 10^{-9}$ we found that the DNM was mostly molecular even while the gas as a whole (in the observed directions) was predominantly atomic, with H-nuclei in atomic form.

In this work we observed CO $J = 1-0$ absorption lines toward six of the thirteen sightlines from Paper I, five of them in the higher-DNM group (Table 4 and Fig. 1). All five of these directions were detected in CO absorption (Fig. 2). Using a conversion between integrated $J = 1-0$ optical depth and CO column density derived earlier from observations of $J = 1-0$ and $J = 2-1$ absorption and emission along comparable sightlines (see Eq. (2) and Fig. 3, and Sect. 4) the observed CO column densities were found to lie in the range 4×10^{13} cm^{-2} $\lesssim N(CO) \lesssim 1.2 \times 10^{15}$ cm^{-2}. This is generally below the expected limit of detectability of extant CO emission surveys given that an integrated CO brightness of $W_{CO} = 1$ K km s^{-1} corresponds to $N(CO) = 10^{15}$ cm^{-2} in diffuse molecular gas (Sect. 4.2). As noted in Paper I, the Planck CO emission foreground maps are, lamentably, hashed in the directions we observe, presumably as the result of point-source removal.

The ratio of $J = 1-0$ integrated optical depths in CO and HCO^+ varies by almost an order of magnitude (Tables 1 and 2). Comparably-wide relative abundance variations are typical of sightlines at moderate reddening seen in UV absorption (Fig. 4) owing to the sensitivity of H_2 and CO column densities to self- and mutual shielding and shielding by dust. To check on the conversions we employed to derive $N(H_2)$ and $N(CO)$ we compared the radio- and UV-determined CO and H_2 column

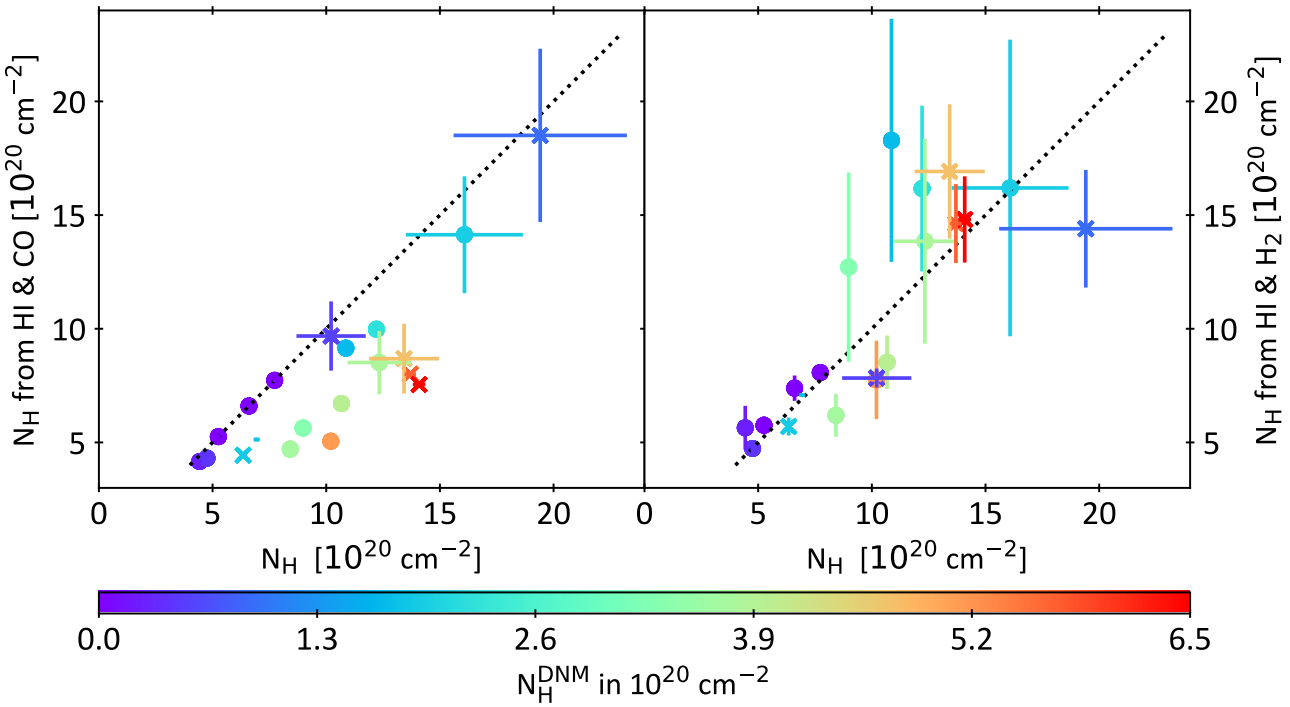


Fig. 8. Comparison of total column density of H-nuclei N(H) derived from the DNM analysis and from observable column densities. The variable plotted along the horizontal axis, $N(\mathrm{H}) = N(\mathrm{HI})|_{\mathrm{cham}} + N(\mathrm{DNM}) + 2W_{\mathrm{CO}}X^0_{\mathrm{CO}}$, is the quantity fitted in the global DNM analysis (Planck Collaboration Int. XXVIII 2015) and is the same in both panels. The vertical axis in each panel is the inferred total hydrogen column density $N(\mathrm{H}) = N(\mathrm{HI})|_{\mathrm{cham}} + 2N(\mathrm{H_2})$ but with $N(\mathrm{H_2})$ taken differently at left and right. At left, N(H) is calculated with $N(\mathrm{H_2}) = W_{\mathrm{CO}}X^0_{\mathrm{CO}}$. At right, N(H) is calculated with $N(\mathrm{H_2}) = N(\mathrm{HCO^+})/3 \times 10^{-9}$ for the sightlines observed in $\mathrm{HCO^+}$ absorption, or using actual measured $N(\mathrm{H_2})$ for the stars with measured $N(\mathrm{H_2})$ and N(CO) (see Fig. 4 and Table 4). The error bars assume ±25% errors in $N(\mathrm{H_2})$ from UV absorption and ±58% errors in the $N(\mathrm{HCO^+})/N(\mathrm{H_2})$ ratio. Stars are marked by crosses and mm-wave targets by filled circles, and all sightlines are color-coded according to N(DNM) as shown at bottom.

densities in Fig. 4, finding the two types of measurements to yield consistent determinations of the run of CO and $\mathrm{H_2}$ column density.

In Fig. 5 we compared N(CO) and $N(\mathrm{HCO^+})$ for the new and existing mm-wave CO absorption measurements, leaving the conversion to $N(\mathrm{H_2})$ implicit. The datasets are consistent and there is nothing unusual about the Chamaeleon measurements, although they lack sightlines with $\mathrm{HCO^+}$ and CO column densities as high as some of those seen earlier (this is also apparent in Fig. 4). Given the equivalence of CO brightness and column density $W_{\mathrm{CO}} \simeq N(\mathrm{CO})/10^{15}$ cm^{-2} in the diffuse molecular gas, the CO–$\mathrm{H_2}$ conversion factor $N(\mathrm{H_2})/W_{\mathrm{CO}}$ is linearly proportional to the CO relative abundance, and $N(\mathrm{H_2})/W_{\mathrm{CO}} \leq 2 \times 10^{20}$ $\mathrm{H_2}$ cm^{-2} (K km s^{-1})$^{-1}$ only when $N(\mathrm{CO})/N(\mathrm{H_2}) \geq 5 \times 10^{-6}$. This is more than twice the mean value observed here: only the red-shifted line toward J0942 has a CO relative abundance high enough that the implied CO-$\mathrm{H_2}$ conversion factor is below $N(\mathrm{H_2})/W_{\mathrm{CO}} = 2 \times 10^{20}$ $\mathrm{H_2}$ cm^{-2} (K km s^{-1})$^{-1}$ (see Table 2 and Fig. 5). High values of the CO-$\mathrm{H_2}$ conversion factor $N(\mathrm{H_2})/W_{\mathrm{CO}}$ were also inferred in Paper I based on the limits to the CO brightness.

The mm-wave CO absorption line chemistry has not been revisited in the 20 yr since the observations of Liszt & Lucas (1998), which is somewhat surprising given the kind of information that is returned. For this reason, and owing to the modest number of sightlines we studied, we somewhat extended the discussion beyond the Chamaeleon region to a more general comparison of CO with $\mathrm{HCO^+}$ and $\mathrm{H_2}$. Beyond the column densities and abundances shown in Figs. 4 and 5, we noted (Fig. 6, Table 3) that the CO FWHM linewidths are consistently about 20% smaller than those seen in the progenitor $\mathrm{HCO^+}$ molecule (0.72 ± 0.22 and 0.87 ± 0.24 km s^{-1} respectively). A comparable difference is seen in CN-bearing species when compared with $\mathrm{HCO^+}$. There is also a ±0.4 km s^{-1} dispersion in the difference of the centroid velocities of $\mathrm{HCO^+}$ and CO (Fig. 7). In Sect. 4 we discussed how the abundances and kinematics of $\mathrm{HCO^+}$, CO and other molecules arise from gas dynamical processes that enhance the formation rate of progenitor ions like $\mathrm{CH^+}$ and $\mathrm{HCO^+}$ and create inhomogeneities that cause linewidth differences.

In Fig. 8 we revisited part of the DNM analysis of Paper I, using a hybrid sample whereby we augmented the ALMA observations with the directly-determined $\mathrm{H_2}$ and CO column densities measured in UV absorption toward 8 bright stars seen toward the Chamaeleon region. As in Paper I we concluded that the DNM in the outskirts of the Chamaeleon complex is mostly molecular, with most H-nuclei in $\mathrm{H_2}$, while the gas overall is primarily atomic.

CO absorption profiles provide more information than just the column density, and consideration of a wider range of CO absorption line observations should help to elucidate the formation of molecules and the presence of DNM and the "dark" gas whose shadows we explored in this work.

Acknowledgements. This paper makes use of the following new ALMA data: ADS/JAO.ALMA#2017.1.00227.S . ALMA is a partnership of ESO (representing its member states), NSF (USA) and NINS (Japan), together with NRC (Canada), NSC and ASIAA (Taiwan), and KASI (Republic of Korea), in cooperation with the Republic of Chile. The Joint ALMA Observatory is operated by ESO, AUI/NRAO and NAOJ. The National Radio Astronomy Observatory is a facility of the National Science Foundation operated under cooperative agreement by Associated Universities, Inc. This work was supported by the French program

"Physique et Chimie du Milieu Interstellaire" (PCMI) funded by the Conseil National de la Recherche Scientifique (CNRS) and Centre National d'Etudes Spatiales (CNES). H.S.L. is grateful to the hospitality of the Observatoire de Paris and La Clemence (1204 CH Geneva) during the initial drafting of this manuscript. We thank the referee for helpful comments that served to clarify the discussion.

References

Burgh, E. B., France, K., & McCandliss, S. R. 2007, ApJ, 658, 446
Crane, P., Lambert, D. L., & Sheffer, Y. 1995, ApJS, 99, 107
Draine, B. T., & Bertoldi, F. 1996, ApJ, 468, 269
Falgarone, E., Pineau Des Forêts, G., & Roueff, E. 1995, A&A, 300, 870
Federman, S. R., Rawlings, J. M. C., Taylor, S. D., & Williams, D. A. 1996, MNRAS, 279, L41
Flower, D. R., & Pineau des Forets, G. 1998, MNRAS, 297, 1182
Gerin, M., Liszt, H., Neufeld, D., et al. 2019, A&A, 622, A26
Glassgold, A. E., & Langer, W. D. 1976, ApJ, 206, 85
Godard, B., Falgarone, E., & Pineau Des Forêts, G. 2009, A&A, 495, 847
Godard, B., Falgarone, E., Gerin, M., Hily-Blant, P., & de Luca, M. 2010, A&A, 520, A20
Godard, B., Falgarone, E., & Pineau des Forêts, G. 2014, A&A, 570, A27
Goldsmith, P. F. 2013, ApJ, 774, 134
Goldreich, P., & Kwan, J. 1974, ApJ, 189, 441
Grenier, I. A., Casandjian, J.-M., & Terrier, R. 2005, Science, 307, 1292
Jenkins, E. B., & Tripp, T. M. 2011, ApJ, 734, 65
Joulain, K., Falgarone, E., Des Forets, G. P., & Flower, D. 1998, A&A, 340, 241
Kalberla, P. M. W., & Haud, U. 2015, A&A, 578, A78
Lambert, D. L., Sheffer, Y., & Crane, P. 1990, ApJ, 359, L19
Lesaffre, P., Pineau des Forêts, G., Godard, B., et al. 2013, A&A, 550, A106
Liszt, H. S. 2007, A&A, 476, 291
Liszt, H. S. 2015, ApJ, 799, 66
Liszt, H. S. 2017, ApJ, 835, 138
Liszt, H. S., & Gerin, M. 2016, A&A, 585, A80
Liszt, H. S., & Lucas, R. 1996, A&A, 314, 917
Liszt, H. S., & Lucas, R. 1998, A&A, 339, 561
Liszt, H. S., & Lucas, R. 2000, A&A, 355, 333
Liszt, H., & Lucas, R. 2001, A&A, 370, 576
Liszt, H. S., & Pety, J. 2012, A&A, 541, A58
Liszt, H. S., Pety, J., & Lucas, R. 2010, A&A, 518, A45
Liszt, H., Gerin, M., & Grenier, I. 2018, A&A, 617, A54
Pan, K., Federman, S. R., Sheffer, Y., & Andersson, B.-G. 2005, ApJ, 633, 986
Pety, J., & Falgarone, É. 2000, A&A, 356, 279
Planck Collaboration XI. 2014, A&A, 571, A11
Planck Collaboration Int. XXVIII. 2015, A&A, 582, A31
Remy, Q., Grenier, I. A., Marshall, D. J., & Casandjian, J. M. 2018, A&A, 611, A51
Schlegel, D. J., Finkbeiner, D. P., & Davis, M. 1998, ApJ, 500, 525
Sheffer, Y., Rogers, M., Federman, S. R., et al. 2008, ApJ, 687, 1075
Sofia, U. J., Lauroesch, J. T., Meyer, D. M., & Cartledge, S. I. B. 2004, ApJ, 605, 272
Sonnentrucker, P., Welty, D. E., Thorburn, J. A., & York, D. G. 2007, ApJS, 168, 58
Sternberg, A., Le Petit, F., Roueff, E., & Le Bourlot, J. 2014, ApJ, 790, 10
Valdivia, V., Godard, B., Hennebelle, P., et al. 2017, A&A, 600, A114
Van Dishoeck, E. F., & Black, J. H. 1986, ApJS, 62, 109
Visser, R., van Dishoeck, E. F., & Black, J. H. 2009, A&A, 503, 323
Weselak, T., Galazutdinov, G., Beletsky, Y., & Krełowski, J. 2009, A&A, 499, 783
Weselak, T., Galazutdinov, G. A., Beletsky, Y., & Krełowski, J. 2010, MNRAS, 402, 1991